


Article

Predicting Compound Coastal Flooding in Embayment-Backed Urban Catchments: Seawall and Storm Drain Implications

Boxiang Tang  and T. W. Gallien * 

Department of Civil and Environmental Engineering, University of California, Los Angeles, CA 90095, USA; bursontung97@ucla.edu

* Correspondence: tgallien@ucla.edu; Tel.: +1-310-825-7731

Abstract: Urban coastal flooding is a global humanitarian and socioeconomic hazard. Rising sea levels will increase the likelihood of hydrologic events interacting with high marine water levels. These compound events may, in turn, nonlinearly interact with urban infrastructure, potentially resulting in more extreme coastal flooding events. Here, an integrated Delft3D-FM based numerical modeling framework is used to concomitantly resolve multi-source flood processes (i.e., high marine water levels, precipitation) and infrastructure (e.g., seawalls, storm drains). Hydrodynamic model results are validated with embayment pressure sensor data and photographic observations from historical events. The impact of tide and precipitation phasing are examined. Multiple storm drain characterizations are presented and evaluated. Results show seawall and storm drain infrastructure is fundamental to accurately resolving spatial and temporal flood dynamics. Importantly, coastal management strategies such as raising seawall elevations to mitigate tidal flooding may exacerbate precipitation-based flooding in low-lying urban regions.

Keywords: coastal flooding; Delft3D-FM; compound flooding; hydrodynamic modeling; infrastructure



Citation: Tang, B.; Gallien, T.W. Predicting Compound Coastal Flooding in Embayment-Backed Urban Catchments: Seawall and Storm Drain Implications. *J. Mar. Sci. Eng.* **2023**, *11*, 1454. <https://doi.org/10.3390/jmse11071454>

Academic Editors: Shaun Williams, Christo Rautenbach, Cyprien Bosserelle and Moritz Wandres

Received: 17 June 2023

Revised: 18 July 2023

Accepted: 20 July 2023

Published: 21 July 2023



Copyright: © 2023 by the authors. Licensee MDPI, Basel, Switzerland. This article is an open access article distributed under the terms and conditions of the Creative Commons Attribution (CC BY) license (<https://creativecommons.org/licenses/by/4.0/>).

1. Introduction

Coastal flooding has been identified as one of the most destructive natural hazards from both social and economic perspectives [1]. Globally, coastal communities are facing a growing challenge from more frequent and extreme coastal flooding events related to sea level rise (e.g., [2,3]), along with climate-induced fluctuations such as seasonal and storm-induced dynamic coastal water levels [4]. Taherkhani et al. [3] projects current 50-year water levels will become annual before 2050 for 70% of the United States coastal region. Similarly, Tebaldi et al. [5] suggests the current 100-year coastal flooding event will occur every 1–10 years for much of the US West Coast by 2050. Along the US West Coast, winter storms often bring high marine water levels along with energetic waves, precipitation and high fluvial flows which may interact nonlinearly, exacerbating flood hazards (e.g., [6]). Although the contributing events themselves are not extreme, the combination may produce extreme flooding [7,8].

Compound events have been identified as an international research priority by the World Climate Research Program (WCRP) Grand Challenge on Weather and Climate Extremes [9]. Compound flooding specifically considers coincident marine and hydrologic events and significantly impacts low-lying urban regions (e.g., [10,11]). Meteorological events (e.g., tropical cyclones, hurricanes) tend to produce wind-driven storm surges and intense precipitation at the coast. Traditional compound flooding studies focused on the combined impacts of marine water levels (often storm-surge-dominated) and fluvial or pluvial flows (e.g., [12–16]). Interaction between riverine discharge and marine water levels have been investigated in the literature (e.g., [16–21]). Notably, however, interactions between surface runoff, storm surge, and direct precipitation are broadly neglected [22,23].

Various flood modeling methodologies have been proposed to assess coastal flooding impacts. Static (i.e., “bathtub”) models rely on a simplistic comparison of extreme water level and land elevations, are easy to implement in GIS software and widely used (e.g., [24,25]). However, these raster-based models neglect hydrodynamics and temporal effects and perform poorly, particularly in complex urban regions with relatively flat terrain [25–29]. More recently, nonlinear shallow-water-based hydrodynamic models of varying complexity have been used to model flooding (e.g., [21,30,31]). Few studies consider urban flow routing and high-resolution flood mapping, because of multiple challenges associated with depicting complex terrain and infrastructure and accurately characterizing transient hydrologic and marine inflows [32]. Critically, there is a paucity of observation and validation data, fundamentally limiting quantitative model evaluation (e.g., [28,32]).

High-quality elevation data are fundamental to accurate flood modeling, and LiDAR data has been recommended for representing topography [33]. However, previous work has shown the limitations of light detection and ranging (LiDAR) digital elevation models (DEMs) for resolving riverine, nearshore bathymetry, or critical hydraulic infrastructure (e.g., [21,27,34]). Real-time kinematic (RTK) surveying (with a known base station) or post-processed GPS observations are recommended to resolve hydraulic features and DEM quality [27,35]. Studies have shown that accurate topo/bathy is critical to quality prediction (e.g., [21]).

The literature also shows the importance of resolving key hydraulic features such as roads, walls, and storm drainage in overland flow modeling (e.g., [27,36–38]). Studies have shown that coastal protection infrastructure can impact local or even regional hydrodynamics (e.g., [39–41]). Notably, coastal flood predictions are highly sensitive to flood defense (i.e., seawall, beach/dune crest) elevations [26,27,42,43]. However, seawall impacts are broadly neglected in compound flooding applications.

Urban flood modeling accuracy is significantly affected by the infiltration and drainage representations [44]. In coastal applications, the storm drain system is linked to embayment water levels. Gallien et al. [27] showed the storm drain system may attenuate flooding via storage and discharge. Shen et al. [45] showed the importance of drainage system elevation since high tailwater can backflow, reducing drainage capacity and thus exacerbating flood impact. Although studies have coupled 1D pipeline models and 2D hydrodynamic models (e.g., [45,46]), limited drainage system data availability has impeded modeling for drainage networks in applications [47,48].

This study develops an integrated modeling approach for concomitantly resolving infrastructure and multi-pathway flood processes, which can be used to quantitatively characterize flood risk in an urbanized backshore. A local-scale (~10 km), highly urbanized coastal region, Sunset Beach in California, serves as a case study (Figure 1). Interactions among different flood pathways can amplify flooding hazard. Here, the joint impacts of precipitation and high marine water levels in an urbanized watershed are considered. A Delft3D-FM based hydrodynamic model explicitly incorporating hydraulic infrastructure (i.e., seawalls, subsurface storm drainage, tide valves) was developed for the study site and validated using water level measurements and photographic reconstructions (e.g., [26,49]). The implications of sea level rise and infrastructure renewal/management are considered through a series of hydrodynamic simulations.

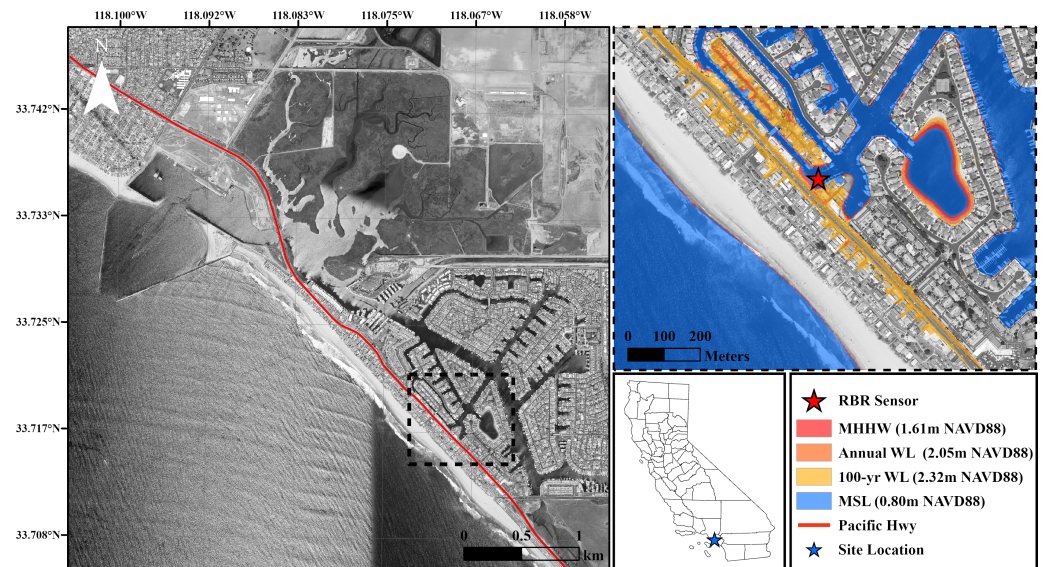


Figure 1. Sunset Beach study site. The enlarged inset highlights topography below (1.63 m NAVD88), annual WL (2.07 m NAVD88 (MHHW)), 100-year 2.34 m NAVD88), and MSL (0.82 m NAVD88 (WL) elevations).

2. Methods

2.1. Site Description

Sunset Beach is a low-lying, infrastructure-rich urbanized region backed by Huntington Harbor (Figure 1). The area is vulnerable to multiple flooding pathways and has experienced several severe flood events (Table 1). These bay-backed urbanized sand spits are typical along the US West Coast and often have substantial public and private infrastructure. The enlarged area of Figure 1 shows the vulnerability to high embayment water levels. Topographic elevations along the main transportation corridor, the Pacific Coast Highway (PCH), range from 1.7 to 2.4 m according to the North American Vertical Datum of 1988 (NAVD88), with many areas below typical spring tide levels (~ 2.07 m NAVD88) and more extreme (~ 2.34 m) water levels [50]. The region has experienced significant flooding from high marine water levels, precipitation, and compound events. Recently, the city's seawall along PCH required elevating (~ 2.43 m NAVD88) to manage tidal flooding. Private seawall elevations are substantially lower (~ 2.24 m NAVD88). Similar to many other low-lying urban coastal regions (e.g., [27]), the storm drainage system is controlled by tide valves, which are closed to prevent back-flooding during high embayment water levels. However, closed tide valves do not allow accumulated precipitation to be drained to the bay which, in turn, causes surface flooding.

Table 1. Historical flooding events recorded in media.

Time	Cause	Source
10 October 2001	High Tide	LA Times
13 December 2012	High Tide	OC Register
25 November 2015	High Tide	OC Register
12 January 2017	High Tide + Rainfall	LA Times
14 February 2019	Rainfall	CBS Los Angeles
28 November 2019	High Tide + Rainfall	OC Register

2.2. Topographic and Bathymetric Data

A seamless bare earth DEM from approximately 2 km offshore through to 2 km inland was prepared for the region, with data summarized in Table 2. Inland topography utilizes a bare earth 2009–2011 CA Coastal Conservancy DEM [51] with 1 m resolution. Offshore bathymetry data are developed from the National Oceanic and Atmospheric Administration

(NOAA) National Geophysical Data Center's tsunami DEM with a resolution of 10 m). Embayment channels and estuary bathymetry are resolved using the U.S. Army Corps of Engineers National Coastal Mapping Program (USACE NCMP) Topobathy LiDAR DEM [52], which includes hydrographic and topographic data depicting the elevations above and below the immediate coastal waters. In areas with poor bathymetric data, estuary and harbor bathymetry were collected using a HYPACK Acoustic Doppler Profiler (ADP) M9 with RTK antenna and from the Southern California Orbit and Permanent array (SoPAC) base station, with expected measurement accuracy of 1% at 10Hz frequency. Critical hydraulic infrastructure such as seawalls and storm drain elevations were resolved with in situ real-time kinematic (RTK) surveys using the SoPAC base station and Stonex900A RTK GPS receiver. The expected vertical error is ~ 2 cm root mean square error (RMSE). The seawall elevation ranged from 2.24 m to 2.72 m NAVD88, depending on location.

Table 2. Data used, in order of priority, for developing seamless DEM.

Priority	Feature	Data Source	Resolution
1	Infrastructure	UCLA RTK Survey	~ 2 cm
2	Estuary and Harbor Bathymetry	UCLA Hydrosurveyor Survey	~ 10 cm
3	Inland Channel	Refined Santa Monica, CA Coastal DEM	1 m
4	Inland Topography	2009–2011 CA Coastal Conservancy LiDAR DEM	1 m
5	Nearshore Bathymetry	2014 USACE NCMP Topobathy LiDAR DEM	1 m
6	Offshore Bathymetry	Santa Monica Tsunami DEM	10 m

2.3. Identifying Compound Flooding Areas

A simple GIS-based analysis was conducted to identify vulnerable regions that may interact during compound flooding events. The tidal overflow region (Figure 2) was estimated using the average seawall elevation contour (2.43 m NAVD88) and encompassed an area of 94,897 m². A flow vector analysis was performed to delineate the rainfall basin where precipitation would concentrate and flow into the tidal overflow region. The precipitation basin totaled 456,971 m², nearly five times larger than the tidal overflow area.



Figure 2. Map of the study site categorized into tidal overflow region and rainfall basin.

2.4. Model

Hydrodynamic models have been widely used to estimate potential flood impacts, including extreme estuarine water levels in compound events (e.g., riverine discharge–tide interactions) and have produced satisfactory results (e.g., [16,19,53–57]). Diffusive wave models are appropriate only in slowly varying flood applications [30,58], and are inadequate for urban applications where abrupt elevation changes force sub- and supercritical flow transitions (e.g., [31,59]). Numerous full nonlinear shallow water models (e.g., AdH, MIKE FLOOD, TUFLOW, DIVAST, BreZo, Delft3D, and TELEMAC) have been successfully implemented in coastal flooding studies (e.g., [16,17,21,27,45,60,61]). For example, Muñoz

et al. [21] simulated and validated flooding from the joint impacts of river discharge and coastal forcing in a complex estuary. Gallien et al. [27] simulated and validated the joint impacts of high marine water levels and wave overtopping in an urban backshore. Similarly, Herdman et al. [17] simulated extreme water levels along the bay–river interface in a highly urbanized estuary and suggested accurate depiction of both fluvial discharge and tide/surge interactions are fundamental to accurately resolving peak water levels and duration.

Delft3D (<http://oss.deltares.nl/web/delft3dfm>, accessed on 22 May 2023) (FM) is an open-source 2D hydrodynamic flexible-mesh numerical model, and has been successfully applied in complex coastal flood modeling applications (e.g., [16,21,53,54,62,63]). Symonds et al. [64] compared Delft3D FM and Mike 21 FM in a complex estuary, and showed both models accurately simulated estuarine hydrodynamics. Delft3D solves full 2D nonlinear shallow water equations with a shock-capturing finite volume approach [65]. Previous literature has shown the full nonlinear shallow water models employing shock capturing schemes (e.g., Galerkin, Godunov) have been shown to accurately route overland flow and handle critical flow transitions caused by urban features (e.g., streets, curbs, and walls) without calibration or parameter tuning (e.g., [11,19,26,43,63,66–69]). Delft3D-FM can incorporate multiple boundary conditions and hydro-meteorological inputs (e.g., marine water levels, riverine discharge, spatially variable precipitation, barometric pressure, wind fields), and can handle multiple flooding pathway interactions required to accurately characterize compound flooding. There are built-in comprehensive hydraulic structures packages (e.g., fixed weirs, source and sink points). Fixed weirs simulating a thin seawall can be defined along mesh edges, blocking flow between two adjacent computational cells when water levels are below a specified fixed weir height without reducing the total wet surface and the volume of the model [17]. Delft3D-FM can incorporate sink and source points to add/extract a discharge to/from the model, and this approach has been successfully implemented in other models to consider drainage or overtopping processes (e.g., [27,70]). Finally, the model supports multi-core parallelism with either open multi-processing (OpenMP) or a message passing interface (MPI) on multiple core machines.

Mesh generation substantially impacts model efficiency and performance [29]. Delft3D-FM supports mixed meshing (i.e., both unstructured and curvilinear grids). Elongated rectangular elements aligned in the flow direction most efficiently convey along channel flows [71]. Refined unstructured grids can be boundary fit, resolving complex geometries with fewer grid total cells, leading to computational efficiency [64,71]. Previous work has suggested hydraulic infrastructure (e.g., artificial dunes, seawalls) is crucial to accurate flood prediction [26,27,34]. Flexible meshing facilitates the complex boundary alignment required to accurately resolve geometrically complex urban regions.

2.5. Model Setup

A site-specific flexible mesh with curvilinear grids in long channels and triangular grids on land was specifically designed to accurately represent the sinuous channels and resolve critical hydraulic infrastructure elevations. Unstructured flexible mesh generation was performed in the Delft RGFRID tool with SEPRAN routines. Final grids were orthogonized to implement the staggered discretization scheme and smoothed to avoid non-convex domains. The modeling domain (i.e., the mesh) covers all above- and below-water terrain near the Sunset Beach region. On land mesh resolution was ~1 m radiating to ~200 m offshore. As shown in Figure 3, all potential key flooding flow paths (e.g., upland channels, streets) were resolved with a minimum of three computational cells, consistent with recommendations for accurately resolving conveyance [72]. Grid nodes representing seawalls or other key hydraulic features were snapped to the seawall location and their elevation were assigned from RTK survey data instead of bare earth DEM.

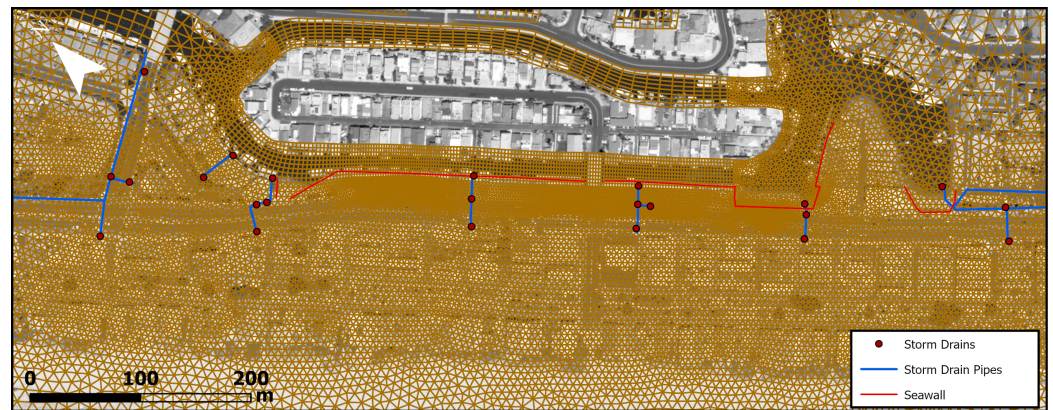


Figure 3. Model domain with highest mesh resolution and underground drainage system.

Bed friction was expressed by Manning's roughness coefficient, and USGS National Land Cover Classifications are usually used to assign corresponding Manning's coefficients (n) in the model (e.g., [73]). A Manning's n value of 0.025 was adopted for open water, road, and vacant land, which are dominant land cover classes for the primary flow regions within the study site. A Manning's n of 0.10 (for medium density residential area) was assigned for nodes representing houses [74]. It is notable that all model roughness coefficients correspond to physical values for a given land cover. No calibration was performed. The time step is essential for modeling rapidly varying flows at a small grid resolution [75]. Delft3D-FM treats the advection term explicitly, and the resulting dynamic time-step limitation is automatically calculated based on the criterion of the Courant–Friedrichs–Lewy condition, with a maximum (default (CFL)) Courant number of 0.7.

The hydrodynamic model was forced by historical offshore water level measurements using six-minute data from the nearest open coast NOAA tide gauge (LA, 9410660) approximately 17 km west of the study site. Prognostic future simulations were forced with the superposition of given sea level rise on a historical NOAA spring tides with 1% non-exceedance probability. Hourly precipitation data were obtained from the closest similar elevation precipitation gauge with a reasonable record length (NOAA's National Climatic Data Center, Long Beach Airport), located 12 km northwest of the study site. Additionally, raw meteorological aerodrome reports (METAR) from the airport were used as a supplement to obtain a total of 72-year hourly rainfall intensity data time series. Rainfall intensity was applied as spatially uniform across the entire domain.

Flood modeling, pre- and post-processing were completed on a personal computer with an Intel Core i7-9750H 2.60 GHz, 6 cores (CPU) processor. Multi-core parallelism was utilized on 4 cores with OpenMP. All model runs included six hours of spin up time, allowing water column velocities to stabilize after being forced at the offshore boundary. Each simulation was 24 h, and modeling took approximately 2 h of real time for each scenario. Spatial flood extent and hydrodynamic time series (i.e., water depth, flow velocity) were output at 20 and 5 min intervals, respectively. ArcGIS and MATLAB were utilized for pre- and post-processing, including the preparation of input files and inundation map visualization.

2.6. Model Validation

In bays or estuaries, water levels may be validated using time series at in situ tide gauge locations (e.g., [76,77]), while for urban coastal flood impacts, field validation data is rarely collected and is emphasized as a significant deficiency in multiple studies (e.g., [27,28,32,49,78–80]). Often “soft data” [49], i.e., depth and extent derived from photos taken during flooding events (e.g., [37,81,82]), or high water marks (e.g., [11,14,21,83]) are used for model performance evaluation in the literature.

An RTK-leveled RBRsolo pressure sensor (hereafter referred to as the sensor) was deployed in the bay (red star shown in Figure 1) to measure the embayment water level

elevation at 1Hz frequency. Pressure data was converted to water depth using an average water density of 1026.0206 kg/m^3 , measured by SonTek CastAway-CTD and corrected for atmospheric pressure measured by a supplementary sub-aerial RBR Solo deployed near the site.

The embayment water level was simulated in the model and compared with the measurement for validation (Figure 4). The sensor was deployed slightly higher than the lower low tide and thus did not capture the lower low tide elevation. The influence of such missing data is negligible since it is the high water level at issue. Validation was conducted only for periods with valid sensor measurements (water level > 0.10 NAVD88). Quantitative comparison is performed with RMSE and Nash–Sutcliffe efficiency ($\text{NSE} \in (-\infty, 1]$) [84] and cross-correlation analysis. The calculated RMSE and NSE are 0.032 m and 0.995, respectively, for the entire simulation period (from 00:00 25 January 2018 to 00:00 1 February 2018, excluding parts with invalid measurements). The cross-correlation lag is 0 s. Peak water levels (higher high water levels) from simulation and measurement are identified and compared, showing an average lag of 1.72 min and an elevation difference of 0.01 m. Validation suggests excellent model performance.

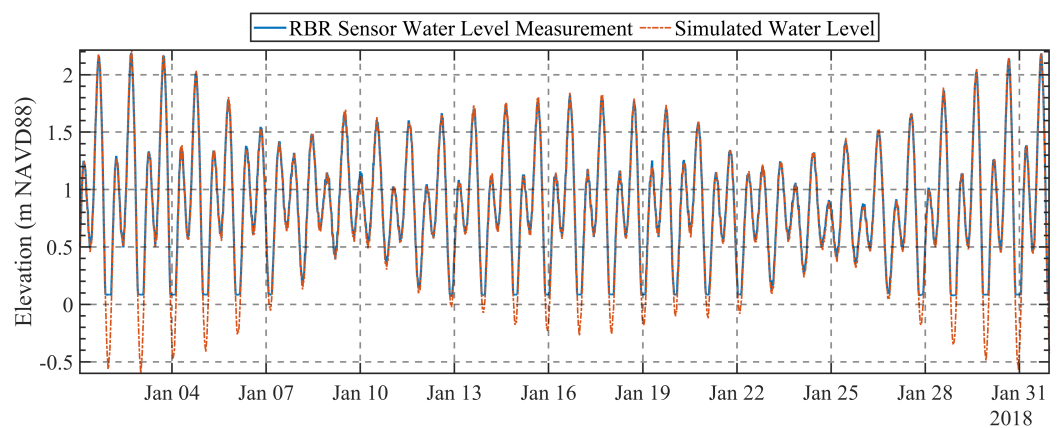


Figure 4. Water level time series at RBR sensor location.

Additionally, similar to Gallien et al. [26] and Smith et al. [49], georeferenced photo documentation provided historical information regarding overland flood extent. A flood on 25 November 2015, resulted from the tidal overflow of bay side seawalls, was reconstructed. Flooding extent was obtained from photographic observations. Photo records capturing flood extent boundaries were found online and identifiable features surveyed with the RTK GPS. The NOAA tide gauge (LA9410660) observed that the extreme water level was at the 90th percentile severity threshold (10% exceedance probability, Table 3) and the overflow mainly occurred near the public seawall (Figure 3). This flooding event was dominated by extreme water level which, therefore, was the only forcing considered in the model. The valve for drainage was closed during the high tide event to prevent back-flooding and thus neglected in the model. The peak water level of 2.32 m NAVD88 was observed around 8:00 25 November 2015 local time. The modeling time is set as from 11:00 24 November 2015 to 17:00 25 November 2015 to model three hours of spin-up time and an entire tidal cycle. As shown in Figure 5, comparison between simulated flood extent and flood boundary derived from in situ photo suggest quality model results.

Table 3. Extreme high water level at NOAA tide gauge (LA9410660).

Percentile	1th	50th	90th	99th
Return Period (year)	1	2	10	100
Water Level	2.07	2.19	2.27	2.34

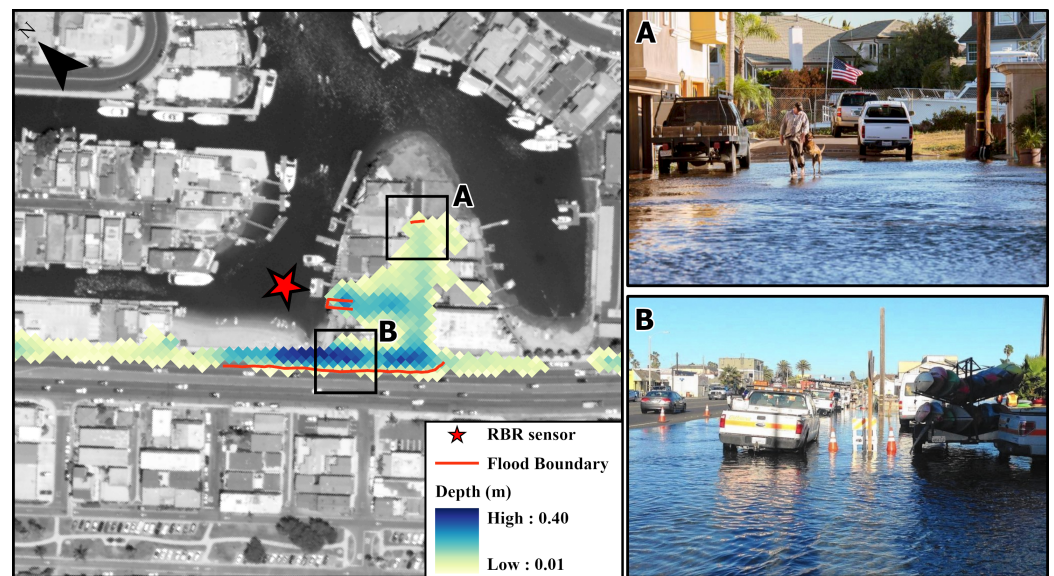


Figure 5. Comparison between estimated flood extent and limited validation data demonstrating a reasonable model capacity. Subplots (A,B) are photos from the Orange County Register (25 November 2015), showing the flood extent boundary at the end of the lane and the Pacific Highway.

2.7. Extreme Event Analysis and Compound Event Design

A total of 23 co-occurrences of high tide and precipitation were identified in overlapping 24-year water level and precipitation data (1997–2021). A sample of ten compound events are shown in Figure 6. The 12 January 2017 event was well-documented in local media. In this study, the compound flood event on 12 January 2017 jointly caused by rainfall and high tide was selected as a base scenario. The peak water level was 2.19 m NAVD88 (50% exceedance probability or every other year, Table 3) and a cumulative precipitation depth of 36.1 mm in 6 h. Additional synthetic scenarios were developed by replacing rainfall input with rainfall derived from marginal probability distribution similar to another study (e.g., [85]). Compound water level and precipitation events commonly rely upon a 24 h rainfall extreme event rainfall which is fit to a probability distribution to estimate rainfall values for various non-exceedance probabilities (e.g., [86–89]). However, this site is highly urbanized (i.e., extensive impervious surface) and is prone to flash flooding on rainfall time scales of minutes to hours. Within this semi-arid region, the 72 years of data show that over 82% of rainfall events occurred in no more than 4 h, and historical enduring rainfall events (>4 h) tend to have small average rainfall intensity (maximum of 15.5 mm per hour).

Shen et al. [45] show that coincident precipitation during high tides can lead to compound flooding, since high tailwater conditions reduce drainage system capacity. In this case, a four hour cumulative rainfall depth, corresponding to the typical tide valve closure duration, is chosen. Annual maximum cumulative rainfall depth derived from a 72-year rainfall record and the best-fitting distribution (Log-Logistic) was selected from 16 distributions (Log-Logistic, Lognormal, Birnbaum-Saunders, Inverse Gaussian, Gamma, Generalized Extreme Value, t Location-Scale, Logistic, Rayleigh, Nakagami, Weibull, Rician, Generalized Pareto, Normal, Exponential, Extreme Value). A Kolmogorov–Smirnov goodness-of-fit test was conducted with the H_0 “the data follow the tested distribution”. Thirteen candidates passed the test at the standard 0.05 level of significance (Log-Logistic, Lognormal, Birnbaum-Saunders, Inverse Gaussian, Gamma, Generalized Extreme Value, t Location-Scale, Logistic, Rayleigh, Nakagami, Weibull, Rician, Normal). The Bayesian information criterion (BIC) [90] is then used to select marginal distribution fits instead of choosing the best fitting directly according to the p -values obtained from hypothesis testing. BIC measures how well a distribution’s estimated parameters fit the sample data, and BIC penalizes for the number of estimated distribution parameters and the data’s sample size

to prevent overfitting. It has been used to select both marginal and copula fits (e.g., [89,91]). Studies have suggested that information-based criteria, including BIC, can help identify the best probability model (e.g., [92,93]). Extreme four-hour cumulative rainfall depths with various return periods (Table 4) were developed from fitted Log-logistic distribution and recommended a precipitation intensity-duration-frequency (IDF) curve for the region [94], respectively.

Table 4. Cumulative rainfall depth (mm) of four-hour design storms with different return period.

Return Period (Year)	Cumulative Depth (mm)	
	IDF Curve	Log-Logistic Distribution
100	68.4	87.6
50	61.8	73.8
25	54.8	62.0
10	44.9	48.8
5	36.7	40.0
2	24.9	28.6

The IDF curve produced generally milder rainfall, especially for more extreme events. Consequently, 4 h design storms from the fitted distribution were chosen to simulate conditions when flash flooding may occur during the valve closure period (high embayment water level duration).

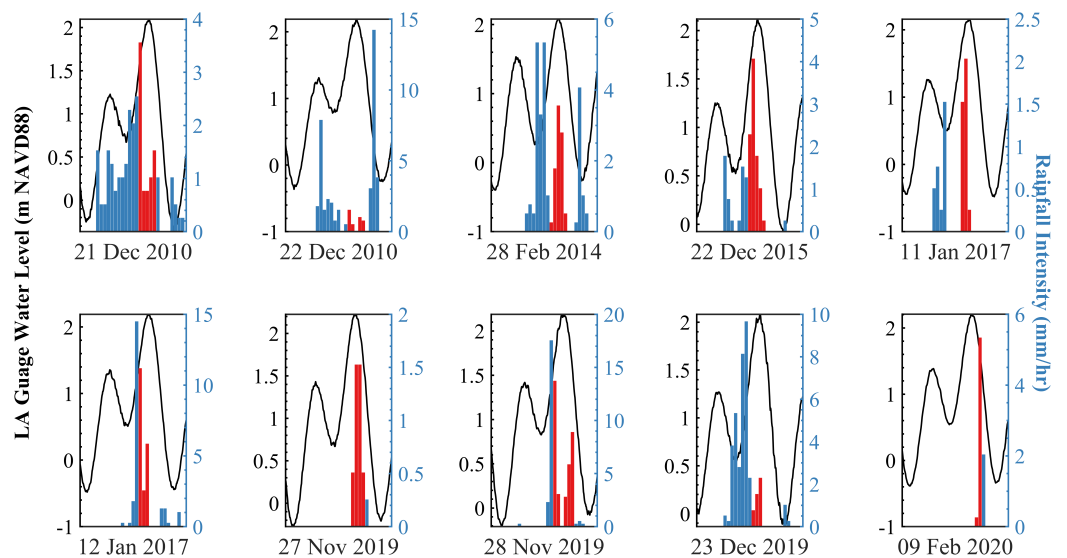


Figure 6. Recent historical concurrences of rainfall and high tide. Water level (black line and left axis) is plotted with contemporary rainfall intensity (bars and right axis). Rainfall that occurred during potential valve closure period is highlighted in red.

2.8. Stormwater Drainage Models

In low-lying urban regions, tide valves are closed to prevent back-flooding through the stormwater network. Pluvial flooding occurs during tide valve closure periods when the network is unable to route precipitation flows to the bay. Valves are usually closed prior to extreme tide and opened after tide falling according to current municipal operations. In municipalities or regions with multiple tide valves, it takes time for maintenance crews to individually open and close each valve. This results in longer-than-necessary storm drain closure periods and, by extension, exacerbates pluvial flooding.

A discounted rainfall rate has previously been used to consider drainage impacts in urban flood modeling (e.g., [37]). Here, the storm drain system is represented using three

alternatives. Constant outflow (CO) withdraws a constant flow at drain inlet locations. The outflow rate was calculated assuming the water level was equal to curb-opening inlet height (e.g., [27]), and the corresponding hydrograph was used as input for the sink points. The weir equation is given by

$$Q = \frac{2}{3} C_v C_d \left(\frac{2}{3} g \right)^{\frac{1}{2}} L H^{\frac{3}{2}} \quad (1)$$

where Q represents the outflow of stormwater, and L and H are length and height of curb-opening inlet [95]. Coefficients C_v and C_d are unity according to the manual. Equation (1) is valid when the inundation depth is less than the inlet height.

An alternative approach, termed iterative outflow (IO), is proposed to compute dynamic outflow rates using either the weir (Equation (1)) or orifice equation, which is given as

$$Q = C_d A (2gH')^{\frac{1}{2}} \quad (2)$$

where A is the area of the curb-opening inlet and H' represents the hydraulic head acting on the center line of the inlet. Coefficient C_d is 0.70. Equation (2) is used when expected water levels are greater than or equal to inlet height. Hydrodynamic simulations were run to simulate 5 min inundation depth time series at the drain inlet, then the weir or orifice equation (dependent on expected depth) was applied to calculate the outflow rate at each time step. An outflow hydrograph was then input as a sink point within the hydrodynamic model. Sinks are incorporated at storm drain locations (Figure 3) in the model with CO and IO representations.

Additionally, a third simplified stormwater drain approach, termed “rainfall reduction” (RR), assumes that stormwater is completely drained (overestimated 100% efficiency) during low tide and that no drainage occurs during high tide. Accordingly, input rainfall intensity is zero during open valve periods. A similar approach was used in urban flood modeling to account for the effect of drainage system and infiltration (e.g., [37]).

3. Results

Single pathway and compound flooding scenarios are simulated to consider flood impacts and infrastructure interaction.

3.1. Historical Compound Flooding Analysis

In this section, historical marine and hydrological forcing from 12 January 2017 are considered. The model is run with tidal forcing only, precipitation forcing only, and as a compound event. Seawall impacts are explicitly considered using elevations interpolated directly from the DEM data (no wall) and RTK survey data (wall). This resulted in six scenarios highlighting the impacts of precipitation, water level, and seawall inclusion (Table 5).

For the univariate tidal flooding analysis (Table 5, T1 and T2), the no-wall scenario shows minor flooding (4350 m²), whereas with the wall included, no flooding is predicted. This is expected since the average seawall elevation is ~2.43 m and is consistent with previous observations that similar 2-year high water levels do not cause flooding in this region because the seawall exceeds the marine water level.

In precipitation-only scenarios (Table 5, P1 and P2), considerable flooding is predicted in both cases, suggesting this site is highly vulnerable to pluvial flooding. The introduction of the seawall increases flooded area and volume slightly by ~3% and ~10% respectively. Rainfall collects in the backshore and is retained by the seawall. Although this particular site shows only a slight increase in maximum flooding extent and water volume, it highlights the importance of including hydraulic features that, at first glance, may be deployed to mitigate alternative flooding drivers.

In compound scenarios (Table 5, C1 and C2), the flood impacts are only slightly higher than those in pluvial flooding scenarios, which is anticipated given that the tidal water

levels are below the average seawall elevation. Although the marine component in this compound event did not cause flooding, the tidally controlled storm drainage was not considered. Subsurface storm drainage system impacts are further investigated in the next section.

Table 5. Quantitative flood impacts for contributing univariate events (i.e., either high marine water level or precipitation) and the historical compound event on 12 January 2017 with and without the seawall resolved.

#	Water Level (m)	Cumulative Rainfall (mm)	Seawall Resolving	Inundation Area (m ²)	Inundation Volume (m ³)	Average Depth (m)	Max Depth (m)
T1	2.19	-	No	4350.0	513.7	0.211	0.592
T2	2.19	-	Yes	-	-	-	-
P1	-	36.1	No	88,681.3	8136.4	0.120	0.596
P2	-	36.1	Yes	91,625.0	8992.9	0.099	0.445
C1	2.19	36.1	No	89,862.5	8514.3	0.161	0.592
C2	2.19	36.1	Yes	91,887.5	9037.0	0.100	0.446

3.2. Subsurface Drainage System

A series of scenarios (Table 6) simulates the historical compound event with various drainage system representations. Scenario C2 (Table 5) focused on compound flooding with the seawall resolved, but did not explicitly consider the storm drainage system and is included here for reference. Scenarios D1, D2, and D3 incorporate the drainage system using various representations, i.e., constant outflow, iterative outflow and reduced rainfall (CO, IO and RR, respectively), with the assumption that the drainage valve is closed only during the 4 h high tide period when the water level exceeds the inlet elevation. Quantitative flood characteristics (flooding area, flooding volume, average and maximum depth) are shown in Table 6 and spatial flood extent for selected scenarios in Figure 7. Unsurprisingly, the no-drainage compound scenario C2 produced the largest average flooding depth (~10 cm) and extent (91,918 m²).

Table 6. Quantitative flood impacts for the historical compound event on 12 January 2017 when modeled with different drainage system and valve operation representations.

#	Water Level (m)	Cumulative Rainfall (mm)	Storm Drain	Inundation Area (m ²)	Inundation Volume (m ³)	Average Depth (m)	Max Depth (m)
C2	2.19	36.1	none	91,887.5	9037.0	0.100	0.446
D1	2.19	36.1	CO	87,193.8	8026.1	0.094	0.423
D2	2.19	36.1	IO	87,237.5	8028.1	0.094	0.422
D3	2.19	8.4	RR	44,881.3	1509.6	0.034	0.286
D4	2.19	36.1 (−2 h)	CO	73,768.8	5385.6	0.073	0.325
D5	2.19	36.1 (+2 h)	CO	91,562.5	8686.8	0.095	0.414
D6	2.19	1.3 (−2 h)	RR	2762.5	42.8	0.092	0.286
D7	2.19	34.0 (+2 h)	RR	89,568.8	8515.5	0.096	0.433

In the reduced rainfall scenario (D3), the precipitation rate was set to zero unless the valve was closed, resulting in a net cumulative rainfall of 8.4 cm. A significantly reduced maximum flood extent (44,881 m²) and depth (~28 cm) are observed. Temporal flood dynamics are in-phase with crucial rainfall and occur only during the valve closure period (red shade in Figure 8). An alternative to the hyetograph reduction is to approximate drainage dynamics using the weir (Equation (1)) or orifice (Equation (2)) equations.

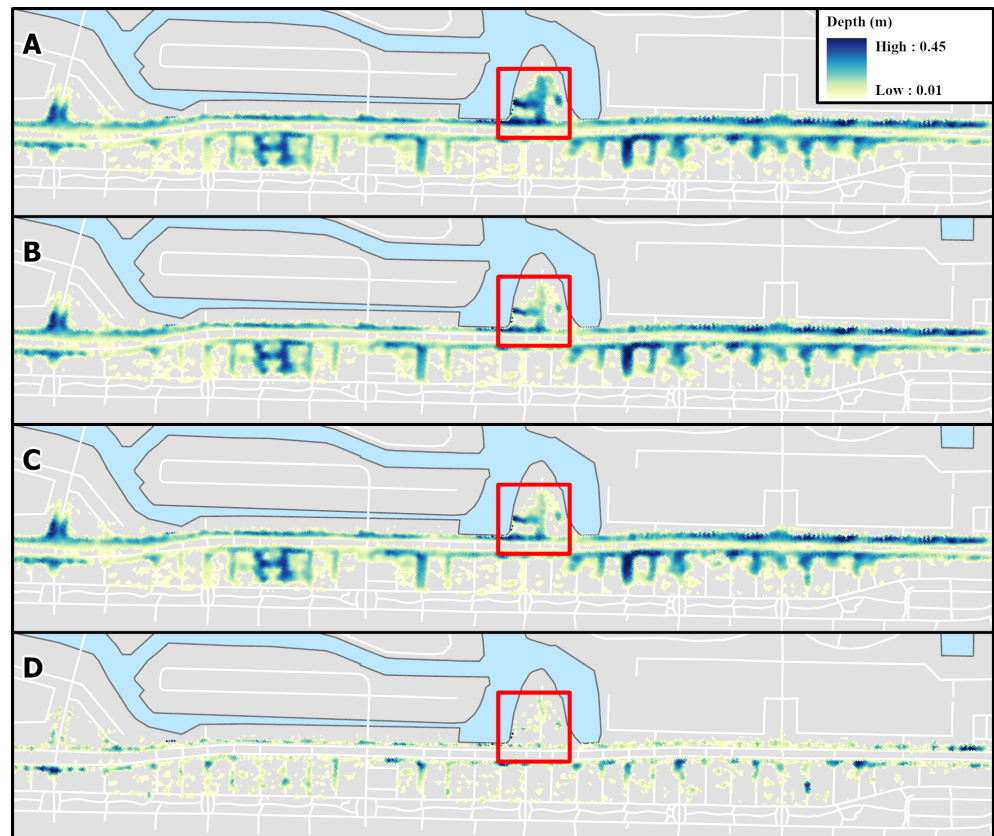


Figure 7. Simulated flood map of the historical event with different drainage system representation. (A) No drainage (scenario C2); (B) constant outflow (scenario D1); (C) iterative outflow (scenario D2); (D) reduced rainfall (scenario D3). The red polygon highlights the area adjacent to the seawall most sensitive to drainage model selection.

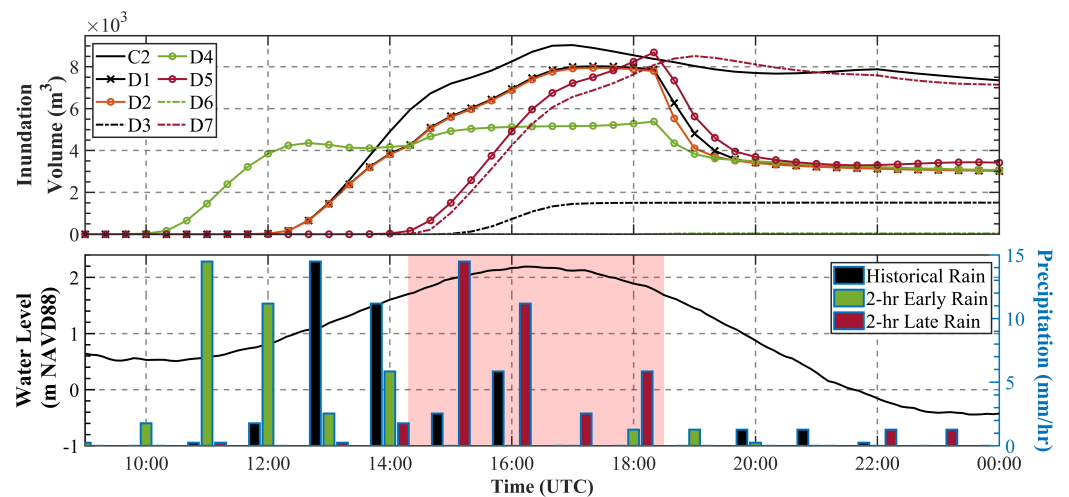


Figure 8. The upper plot shows the temporal flood dynamics, while the lower plot shows the corresponding marine and hydrological forcing. The tide valve closure period is highlighted with red shading.

In Table 6, D2 (CO) uses only Equation (1), while the more complex D3 (IO) representation (Table 6) chooses either Equation (1) or Equation (2), depending on water level estimates extracted from antecedent model runs (see Section 2.8). Generally, both CO and IO approaches produce slightly lower flood impacts compared to the no-drainage scenario (Table 6), and depth differences are observed near the public seawall (red rectangle in Figure 7). Temporal flood dynamics, however, differ substantially (Figure 8).

When marine water levels are low and stormwater discharges through the storm drain system, the flooding volume decreases to a low value for both the constant outflow (D1) and iterative outflow (D2) scenarios after 18:30 UTC, while that of the C2 scenario (without drainage) plateaus after the rainfall. Interestingly, all three drainage system representations resulted in underestimation of the residual flood impact. Scenario C2 (without drainage) most closely matched field observations, suggesting that tide valves were likely closed for longer than the required time.

4. Discussion

Rising sea levels will increase the number of hours tide valves must be closed. A simple superposition of sea level rise on historical water levels (Figure 9), suggests substantial increases in compound events. Precipitation phasing and potential adaptation strategies (e.g., elevating seawalls) must be considered to accurately characterize compound flooding events.

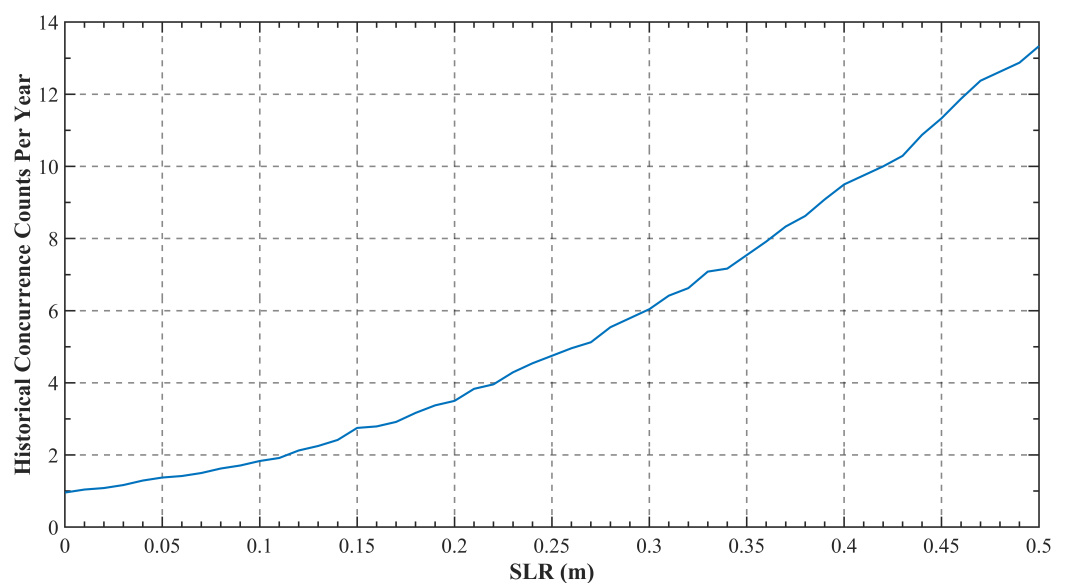


Figure 9. Annual expected future compound events in the Sunset Beach region.

4.1. Precipitation and Tide Phasing

Results suggest that precipitation and water level phasing is critical to accurate compound flood prediction. If a compound flood is simulated where the tide valves are assumed closed only for water levels > 1.68 m, flooding depends entirely on the precipitation timing relative to the high tide. The impact of precipitation and high-tide phasing on flood impact was investigated by shifting the historical storm two hours earlier and later for CO and RR models (Figure 8; Table 6, scenarios D4–D8). In the early arrival time (Figure 8, D4, D6), nearly all rainfall occurs outside of the valve closure period and flood peaks are mitigated, while the later arrival time (Figure 8, D5, D7) brought more rainfall during the valve closure period and exacerbated flooding. In the constant outflow case, late storm arrival increased flood volume by $\sim 8\%$ and area by $\sim 5\%$, while early arrival significantly decreased both flooding volume and area ($\sim 33\%$ and $\sim 15\%$) (Figure 8 and Table 6, D4, D5). Simplified RR representation is more sensitive to phasing, since it overestimates the drainage efficiency. In the early arrival scenario (Figure 8 and Table 6, D6), only 1.3 mm of precipitation occurs during valve closure, resulting in extremely low inundation area and volumes. Clearly, the phasing of the hyetograph and tide are critical to accurate flood prediction. Although the reduced rainfall method is the simplest to implement, both flood impacts and dynamics are not well-represented.

4.2. Seawall Impacts

The 100-year water level is expected to become annual in this century [3,5]. Increasing sea levels will necessitate elevated seawalls to mitigate tidal flooding. Critically, however, the seawall may retain tidal overflow and interact with precipitation, potentially exacerbating both marine and pluvial flooding. Given that the current seawall elevation tidal overflow begins at ~ 2.35 m NAVD88 (essentially, the current 100-year return period), resulting in a relatively small maximum flood extent of $18,256 \text{ m}^2$ (Figure 10A), a 10 cm increase in water level to 2.45 m results in a four-fold increase in a flooded area of $77,100 \text{ m}^2$, whereas a 2.55 m water level results in a six-fold increase in flooded area of $108,887 \text{ m}^2$ (Figure 10A). From a volume perspective, a 2.35 m tide produces a relatively small maximum inundation of 1984 m^3 (Figure 10C). A 10 cm increase in water level to 2.45 m results in a nearly six-fold increase in inundation ($11,603 \text{ m}^3$), whereas a 2.55 m water level results flooded area of $24,800 \text{ m}^3$, more than an order of magnitude compared to the current 100-year water level (Figure 10C). Elevating the seawall to a uniform 2.5 m prohibits tidal overflow for marine water levels below this threshold (Figure 10B,D). However, the elevated seawall may offer only limited protection for future extreme tides. In this case, a high tide of 5 cm over the elevated wall (2.55 m) essentially fills the backshore (Figure 10D) and provides only a marginal benefit when compared to the current seawall ($20,592$ vs. $24,800 \text{ m}^3$, respectively).

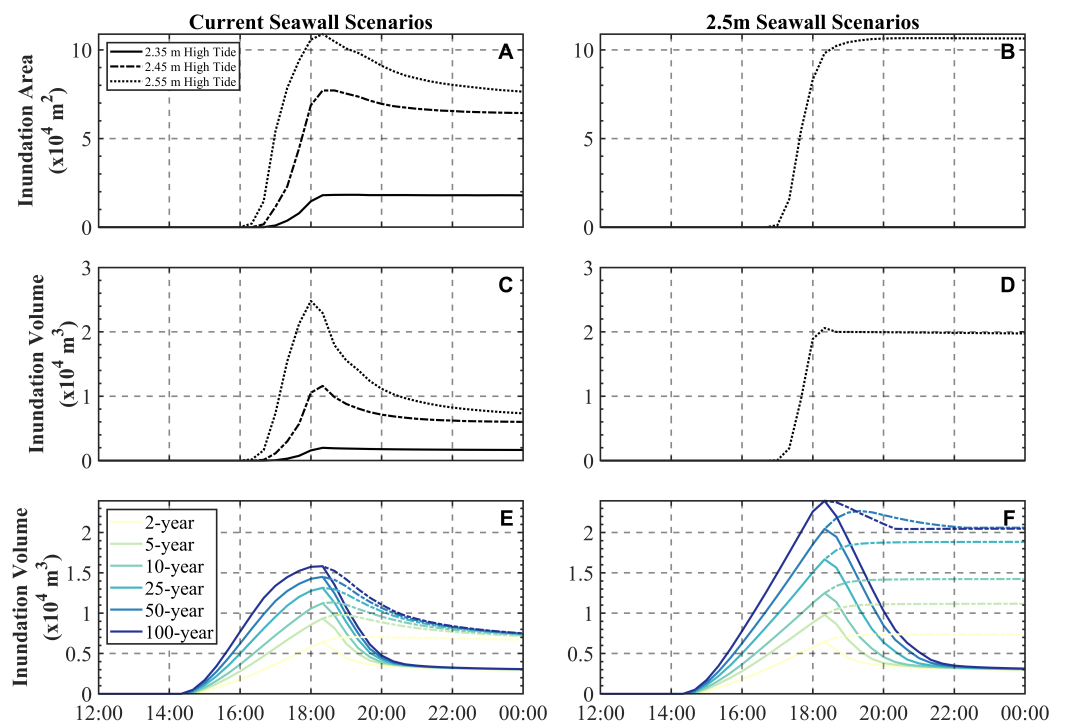


Figure 10. Tidal overflow flooding extent and volume for the current seawall (A,C) and the 2.5 m seawall (B,D). Compound flood dynamics for various precipitation return periods with drainage (solid lines) and without (dashed lines) drainage for the current seawall (E), and the 2.5 m seawall (F). The first 12 simulation hours are not shown, since no flooding is observed.

From a pluvial perspective, simple analysis (Section 2.3), suggests a rainfall event with a cumulative depth of 25 mm could completely fill the basin, assuming all precipitation flows concentrate in the low-elevation tidal overflow region. This cumulative rainfall depth is similar to a 2-year return period precipitation event. This enough-to-fill cumulative rainfall depth suggests that heavier events may simply overflow the seawall and not cause additional flooding in this sub-basin. This hypothesis was tested with synthetic compound scenarios composed of the historical high tide on 12 January 2017 and storm designs of different return periods (Section 2.7, Table 4), assuming the four-hour storm occurred during the valve closure period and thus no drainage of stormwater during the rainfall.

Multiple scenarios were created by running synthetic compound flooding events with the current and an elevated uniform 2.5 m NAVD88 seawall along with the CO drainage representation (i.e., drainage occurs at marine water level values below 1.68 m NAVD88, when tide valves are open).

Seawall impacts on pluvial flooding are shown in Figure 10E,F, with (solid lines) and without (dashed lines) drainage. Here, only total inundation volume for the sub-basin adjacent to the wall is considered, since uniform precipitation causes isolated non-hydraulically connected low spots to accumulate water. No drainage scenarios (dashed lines) represent situations when tide valves are closed during a compound event. Although peak flood volumes for a given return period with the current seawall are identical with and without drainage (Figure 10E), flood duration is substantially decreased with drainage (solid lines). Simply elevating the seawall to a constant 2.5 m results in substantial pluvial flooding increases (Figure 10F). The average inundation volume for the 25-year return period with the 2.5 m seawall is similar to the 100-year inundation volume with the current seawall (Figure 10E,F). More extreme events showed flood volumes converge to the sub-basin volumes constrained by the seawall, suggesting the overflow sub-basin saturates. For example, the 100-year precipitation event produces only a marginally higher flood peak than the 50-year, though the peak timing is shifted by approximately one hour (Figure 10F). These results suggest that elevating seawalls to mitigate marine flooding may exacerbate pluvial flooding. Notably, as sea levels rise, storm drains will be closed more frequently and over longer periods, substantially increasing both future flood extent and duration.

5. Conclusions

Sea level rise will require fortification of defended communities, and previously undefended regions may need to adopt marine water level flood defenses (e.g., seawalls) which may amplify other flood sources (precipitation, waves) impacts. Compound flooding, in particular, may interact nonlinearly with infrastructure (e.g., [32,45]). Resolving these interactions is fundamental to accurately predicting evolving coastal flood risks. Accurate compound coastal flood modeling requires careful site evaluation and hydraulic infrastructure inclusion. For example, tidal flooding and precipitation basins may differ. Inclusion of precipitation basins interacting with embayment marine water levels through tidal overflow or storm drain outfalls is critical to accurately assessing compound flood risk. Hydraulic infrastructure plays a key role in both spatial and temporal urban flood dynamics.

Seawall and storm drainage inclusion is critical to accurate compound flooding modeling in low-lying urban backshores. Neglecting seawalls (Table 5, T1–T2) results in substantial overestimation of high marine water flooding and mild underestimation of precipitation flooding (Table 5, P1–P2). However, when the seawall is raised slightly to 2.5 m, a 51.3% increase in inundation volume is observed for the compound event with 100-year rainfall (Figure 10E,F), while the flood duration increases by over an hour. Similarly, storm drain representation significantly impacts both the spatial and temporal flood characteristics. Exclusion of the drainage system predicted the largest and deepest floods. The highly simplified reduced rainfall method predicted the lowest flooding depths and extents while either the constant outflow or more sophisticated iterative approach provided similar extents and depths. Neglecting the drainage system leads to a slight overestimation of flood extent and depth (Table 6, C1, D1–D3). Maximum inundation volume increases 12.6% from 8026 to 9037 m³. Notably, however, this is highly dependent on the phasing of the high marine tailwater and precipitation (Table 6, D1, D4–D5) where maximum inundation volumes vary up to 85%. Precipitation is expected to intensify (e.g., [96]) while rising sea levels will necessitate longer valve closure times, magnifying flood extent, depth and duration in low-lying, protected urban communities.

Sea level rise will amplify coastal flood risk along multiple pathways. Here, even a moderate sea level rise (40 cm) increases the likelihood of a compound flooding event by an order of magnitude. Coastal management interventions, such as elevating seawalls to mitigate tidal flooding, amplify compound flooding events by retaining water that would have previously overflowed the (lower) seawall and drained to the bay. In this particular case, a 10 cm rise in sea levels doubles the likelihood of pluvial flooding from precipitation occurring while tide valves are closed and storm drains cannot function. Pumping activities may serve to mitigate this; however, as compound coastal flooding increases in both frequency and intensity, coastal management's ability to respond to simultaneously distributed flooding will be challenged.

Although this study was limited to a single demonstration site, the implications are likely similar for other bay- (or harbor)-backed sand spits common to the US West Coast and present throughout the world. These results are not applicable to high-elevation coastal regions, headlands, cliffs, or land-backed beaches unaffected by high tailwater conditions. The present study considers only the concurrence of precipitation and high marine water levels. Compound flooding may be driven by other spatiotemporally variable flows, such as wave overtopping and emergent groundwater, which deserve consideration in future studies.

Lastly, observations are critical to accurately predicting compound flooding. A lack of spatial and hydrodynamic in situ observations has limited high accuracy compound coastal flood validation. Flood extent, a common validation observation, cannot partition the impacts of precipitation versus marine flooding. Quantitative infrastructure mapping and in situ temporal (depth, velocity, salinity) and spatial observations are recommended for advancing complex urban coastal flooding prediction.

Author Contributions: B.T.: methodology, software, validation, formal analysis, investigation, data curation, writing—original draft, writing—review and editing, visualization. T.W.G.: conceptualization, writing—original draft, writing—review and editing, resources, supervision, project administration, funding acquisition. All authors have read and agreed to the published version of the manuscript.

Funding: This work has been supported by the US Coastal Research Program under contract W912HZ-20-200-004, California Department of Parks and Recreation contact number C1670006 and UCLA startup funds.

Institutional Review Board Statement: Not applicable.

Informed Consent Statement: Not applicable.

Data Availability Statement: All mesh and model data are available upon request.

Acknowledgments: This work has been supported by the US Coastal Research Program under contract W912HZ-20-200-004, California Department of Parks and Recreation contact numbers C1670006 and C22820007, and UCLA startup funds. The US Coastal Research Program (USCRP) is administered by the US Army Corps of Engineers® (USACE), Department of Defense. The content of the information provided in this publication does not necessarily reflect the position or the policy of the government, and no official endorsement should be inferred. The authors acknowledge the USACE and USCRP's support of their effort to strengthen coastal academic programs and address coastal community needs in the United States. Any opinions, findings, conclusions or recommendations expressed in this material are those of the author(s) and do not necessarily reflect the views of the agencies supporting the work. We would like to acknowledge Maria Winters for collecting the pressure sensor data used for validation, and Xiaoyu Ma for compiling site flooding history.

Conflicts of Interest: The authors declare no conflict of interest.

Abbreviations

The following abbreviations are used in this manuscript:

BIC	Bayesian information criterion
CO	Constant outflow
DEM	Digital elevation model
IDF	Intensity-duration-frequency
IO	Iterative outflow
LiDAR	Light detection and ranging
NAVD88	North American Vertical Datum of 1988
NSE	Nash–Sutcliffe efficiency
NOAA	National Oceanic and Atmospheric Administration
PCH	Pacific Coast Highway
RMSE	Root mean square error
RR	Reduced rainfall
RTK	Real-time kinematic
USGS	United States Geological Survey

References

1. NASEM. *Framing the Challenge of Urban Flooding in the United States*; National Academies of Sciences, Engineering, and Medicine and Others; National Academies Press: Washington, DC, USA, 2019.
2. Vitousek, S.; Barnard, P.L.; Fletcher, C.H.; Frazer, N.; Erikson, L.; Storlazzi, C.D. Doubling of coastal flooding frequency within decades due to sea-level rise. *Sci. Rep.* **2017**, *7*, 1399. [[CrossRef](#)] [[PubMed](#)]
3. Taherkhani, M.; Vitousek, S.; Barnard, P.L.; Frazer, N.; Anderson, T.R.; Fletcher, C.H. Sea-level rise exponentially increases coastal flood frequency. *Sci. Rep.* **2020**, *10*, 6466. [[CrossRef](#)] [[PubMed](#)]
4. Barnard, P.L.; van Ormondt, M.; Erikson, L.H.; Eshleman, J.; Hapke, C.; Ruggiero, P.; Adams, P.N.; Foxgrover, A.C. Development of the Coastal Storm Modeling System (CoSMoS) for predicting the impact of storms on high-energy, active-margin coasts. *Nat. Hazards* **2014**, *74*, 1095–1125. [[CrossRef](#)]
5. Tebaldi, C.; Strauss, B.H.; Zervas, C.E. Modelling sea level rise impacts on storm surges along US coasts. *Environ. Res. Lett.* **2012**, *7*, 014032. [[CrossRef](#)]
6. Moftakhari, H.R.; Salvadori, G.; AghaKouchak, A.; Sanders, B.F.; Matthew, R.A. Compounding effects of sea level rise and fluvial flooding. *Proc. Natl. Acad. Sci. USA* **2017**, *114*, 9785–9790. [[CrossRef](#)]
7. Seneviratne, S.; Nicholls, N.; Easterling, D.; Goodess, C.; Kanae, S.; Kossin, J.; Luo, Y.; Marengo, J.; McInnes, K.; Rahimi, M.; et al. Changes in climate extremes and their impacts on the natural physical environment. In *Managing the Risks of Extreme Events and Disasters to Advance Climate Change Adaptation*; Cambridge University Press: Cambridge, UK, 2012.
8. Field, C.B.; Barros, V.; Stocker, T.F.; Dahe, Q. *Managing the Risks of Extreme Events and Disasters to Advance Climate Change Adaptation: Special Report of the Intergovernmental Panel on Climate Change*; Cambridge University Press: Cambridge, UK, 2012.
9. Zscheischler, J.; Westra, S.; Van Den Hurk, B.J.; Seneviratne, S.I.; Ward, P.J.; Pitman, A.; AghaKouchak, A.; Bresch, D.N.; Leonard, M.; Wahl, T.; et al. Future climate risk from compound events. *Nat. Clim. Chang.* **2018**, *8*, 469. [[CrossRef](#)]
10. Ganguli, P.; Merz, B. Extreme coastal water levels exacerbate fluvial flood hazards in Northwestern Europe. *Sci. Rep.* **2019**, *9*, 13165. [[CrossRef](#)]
11. Stephens, T.A.; Savant, G.; Sanborn, S.C.; Wallen, C.M.; Roy, S. Monolithic multiphysics simulation of compound flooding. *J. Hydraul. Eng.* **2022**, *148*, 05022003. [[CrossRef](#)]
12. Wahl, T.; Jain, S.; Bender, J.; Meyers, S.D.; Luther, M.E. Increasing risk of compound flooding from storm surge and rainfall for major US cities. *Nat. Clim. Chang.* **2015**, *5*, 1093. [[CrossRef](#)]
13. Bevacqua, E.; Maraun, D.; Voudoukas, M.I.; Voukouvalas, E.; Vrac, M.; Mentaschi, L.; Widmann, M. Higher probability of compound flooding from precipitation and storm surge in Europe under anthropogenic climate change. *Sci. Adv.* **2019**, *5*, eaaw5531. [[CrossRef](#)]
14. Gori, A.; Lin, N.; Smith, J. Assessing Compound Flooding from Landfalling Tropical Cyclones on the North Carolina Coast. *Water Resour. Res.* **2020**, *56*, e2019WR026788. [[CrossRef](#)]
15. Song, H.; Kuang, C.; Gu, J.; Zou, Q.; Liang, H.; Sun, X.; Ma, Z. Nonlinear tide-surge-wave interaction at a shallow coast with large scale sequential harbor constructions. *Estuar. Coast. Shelf Sci.* **2020**, *233*, 106543. [[CrossRef](#)]
16. Nederhoff, K.; Saleh, R.; Tehranirad, B.; Herdman, L.; Erikson, L.; Barnard, P.L.; Van der Wegen, M. Drivers of extreme water levels in a large, urban, high-energy coastal estuary—A case study of the San Francisco Bay. *Coast. Eng.* **2021**, *170*, 103984. [[CrossRef](#)]
17. Herdman, L.; Erikson, L.; Barnard, P. Storm surge propagation and flooding in small tidal rivers during events of mixed coastal and fluvial influence. *J. Mar. Sci. Eng.* **2018**, *6*, 158. [[CrossRef](#)]

18. Ward, P.J.; Couasnon, A.; Eilander, D.; Haigh, I.D.; Hendry, A.; Muis, S.; Veldkamp, T.I.; Winsemius, H.C.; Wahl, T. Dependence between high sea-level and high river discharge increases flood hazard in global deltas and estuaries. *Environ. Res. Lett.* **2018**, *13*, 084012. [\[CrossRef\]](#)
19. Moftakhari, H.; Schubert, J.E.; AghaKouchak, A.; Matthew, R.A.; Sanders, B.F. Linking statistical and hydrodynamic modeling for compound flood hazard assessment in tidal channels and estuaries. *Adv. Water Resour.* **2019**, *128*, 28–38. [\[CrossRef\]](#)
20. Couasnon, A.; Eilander, D.; Muis, S.; Veldkamp, T.I.; Haigh, I.D.; Wahl, T.; Winsemius, H.C.; Ward, P.J. Measuring compound flood potential from river discharge and storm surge extremes at the global scale. *Nat. Hazards Earth Syst. Sci.* **2020**, *20*, 489–504. [\[CrossRef\]](#)
21. Muñoz, D.; Moftakhari, H.; Moradkhani, H. Compound Effects of Flood Drivers and Wetland Elevation Correction on Coastal Flood Hazard Assessment. *Water Resour. Res.* **2020**, *56*, e2020WR027544. [\[CrossRef\]](#)
22. Santiago-Collazo, F.L.; Bilskie, M.V.; Hagen, S.C. A comprehensive review of compound inundation models in low-gradient coastal watersheds. *Environ. Model. Softw.* **2019**, *119*, 166–181. [\[CrossRef\]](#)
23. Xu, K.; Wang, C.; Bin, L. Compound flood models in coastal areas: A review of methods and uncertainty analysis. *Nat. Hazards* **2022**, *116*, 469–496. [\[CrossRef\]](#)
24. Hinkel, J.; Lincke, D.; Vafeidis, A.T.; Perrette, M.; Nicholls, R.J.; Tol, R.S.; Marzeion, B.; Fettweis, X.; Ionescu, C.; Levermann, A. Coastal flood damage and adaptation costs under 21st century sea-level rise. *Proc. Natl. Acad. Sci. USA* **2014**, *111*, 3292–3297. [\[CrossRef\]](#) [\[PubMed\]](#)
25. Teng, J.; Vaze, J.; Dutta, D.; Marvanek, S. Rapid inundation modelling in large floodplains using LiDAR DEM. *Water Resour. Manag.* **2015**, *29*, 2619–2636. [\[CrossRef\]](#)
26. Gallien, T.; Schubert, J.; Sanders, B. Predicting tidal flooding of urbanized embayments: A modeling framework and data requirements. *Coast. Eng.* **2011**, *58*, 567–577. [\[CrossRef\]](#)
27. Gallien, T.; Sanders, B.; Flick, R. Urban coastal flood prediction: Integrating wave overtopping, flood defenses and drainage. *Coast. Eng.* **2014**, *91*, 18–28. [\[CrossRef\]](#)
28. Ramirez, J.A.; Lichter, M.; Coulthard, T.J.; Skinner, C. Hyper-resolution mapping of regional storm surge and tide flooding: Comparison of static and dynamic models. *Nat. Hazards* **2016**, *82*, 571–590. [\[CrossRef\]](#)
29. Teng, J.; Jakeman, A.J.; Vaze, J.; Croke, B.F.; Dutta, D.; Kim, S. Flood inundation modelling: A review of methods, recent advances and uncertainty analysis. *Environ. Model. Softw.* **2017**, *90*, 201–216. [\[CrossRef\]](#)
30. Neal, J.; Villanueva, I.; Wright, N.; Willis, T.; Fewtrell, T.; Bates, P. How much physical complexity is needed to model flood inundation? *Hydrol. Process.* **2012**, *26*, 2264–2282. [\[CrossRef\]](#)
31. Costabile, P.; Costanzo, C.; Macchione, F. Performances and limitations of the diffusive approximation of the 2-d shallow water equations for flood simulation in urban and rural areas. *Appl. Numer. Math.* **2017**, *116*, 141–156. [\[CrossRef\]](#)
32. Gallien, T.W.; Kalligeris, N.; Delisle, M.P.C.; Tang, B.X.; Lucey, J.T.; Winters, M.A. Coastal flood modeling challenges in defended urban backshores. *Geosciences* **2018**, *8*, 450. [\[CrossRef\]](#)
33. Sanders, B.F. Evaluation of on-line DEMs for flood inundation modeling. *Adv. Water Resour.* **2007**, *30*, 1831–1843. [\[CrossRef\]](#)
34. Gallien, T. Validated coastal flood modeling at Imperial Beach, California: Comparing total water level, empirical and numerical overtopping methodologies. *Coast. Eng.* **2016**, *111*, 95–104. [\[CrossRef\]](#)
35. Didier, D.; Bernatchez, P.; Boucher-Brossard, G.; Lambert, A.; Fraser, C.; Barnett, R.L.; Van-Wierst, S. Coastal flood assessment based on field debris measurements and wave runup empirical model. *J. Mar. Sci. Eng.* **2015**, *3*, 560–590. [\[CrossRef\]](#)
36. Fewtrell, T.J.; Duncan, A.; Sampson, C.C.; Neal, J.C.; Bates, P.D. Benchmarking urban flood models of varying complexity and scale using high resolution terrestrial LiDAR data. *Phys. Chem. Earth Parts A/B/C* **2011**, *36*, 281–291. [\[CrossRef\]](#)
37. Wang, Y.; Chen, A.S.; Fu, G.; Djordjević, S.; Zhang, C.; Savić, D.A. An integrated framework for high-resolution urban flood modelling considering multiple information sources and urban features. *Environ. Model. Softw.* **2018**, *107*, 85–95. [\[CrossRef\]](#)
38. Bates, P.D.; Quinn, N.; Sampson, C.; Smith, A.; Wing, O.; Sosa, J.; Savage, J.; Olcese, G.; Neal, J.; Schumann, G.; et al. Combined modeling of US fluvial, pluvial, and coastal flood hazard under current and future climates. *Water Resour. Res.* **2021**, *57*, e2020WR028673. [\[CrossRef\]](#)
39. Pelling, H.E.; Green, J.M. Impact of flood defences and sea-level rise on the European Shelf tidal regime. *Cont. Shelf Res.* **2014**, *85*, 96–105. [\[CrossRef\]](#)
40. Lee, S.B.; Li, M.; Zhang, F. Impact of sea level rise on tidal range in Chesapeake and Delaware Bays. *J. Geophys. Res. Oceans* **2017**, *122*, 3917–3938. [\[CrossRef\]](#)
41. Jia, G.; Wang, R.Q.; Stacey, M.T. Investigation of impact of shoreline alteration on coastal hydrodynamics using Dimension REDuced Surrogate based Sensitivity Analysis. *Adv. Water Resour.* **2019**, *126*, 168–175. [\[CrossRef\]](#)
42. Wadey, M.P.; Nicholls, R.J.; Hutton, C. Coastal flooding in the Solent: An integrated analysis of defences and inundation. *Water* **2012**, *4*, 430–459. [\[CrossRef\]](#)
43. Huang, W.; Zhang, Y.J.; Liu, Z.; Yu, H.C.; Liu, Y.; Lamont, S.; Zhang, Y.; Hirpa, F.; Li, T.; Baker, B.; et al. Simulation of compound flooding in Japan using a nationwide model. *Nat. Hazards* **2023**, *117*, 2693–2713. [\[CrossRef\]](#)
44. Leandro, J.; Schumann, A.; Pfister, A. A step towards considering the spatial heterogeneity of urban key features in urban hydrology flood modelling. *J. Hydrol.* **2016**, *535*, 356–365. [\[CrossRef\]](#)
45. Shen, Y.; Morsy, M.M.; Huxley, C.; Tahvildari, N.; Goodall, J.L. Flood risk assessment and increased resilience for coastal urban watersheds under the combined impact of storm tide and heavy rainfall. *J. Hydrol.* **2019**, *579*, 124159. [\[CrossRef\]](#)

46. Shi, S.; Yang, B.; Jiang, W. Numerical simulations of compound flooding caused by storm surge and heavy rain with the presence of urban drainage system, coastal dam and tide gates: A case study of Xiangshan, China. *Coast. Eng.* **2022**, *172*, 104064. [CrossRef]
47. Zhang, S.; Pan, B. An urban storm-inundation simulation method based on GIS. *J. Hydrol.* **2014**, *517*, 260–268. [CrossRef]
48. Liu, L.; Liu, Y.; Wang, X.; Yu, D.; Liu, K.; Huang, H.; Hu, G. Developing an effective 2-D urban flood inundation model for city emergency management based on cellular automata. *Nat. Hazards Earth Syst. Sci.* **2015**, *15*, 381–391. [CrossRef]
49. Smith, R.A.; Bates, P.D.; Hayes, C. Evaluation of a coastal flood inundation model using hard and soft data. *Environ. Model. Softw.* **2012**, *30*, 35–46. [CrossRef]
50. NOAA. Extreme Water Levels 9410660 Los Angeles, CA, 2023. National Oceanic and Atmospheric Administration Website. Available online: https://tidesandcurrents.noaa.gov/est/est_station.shtml?stnid=9410660 (accessed on 22 May 2023).
51. NOAA. 2009–2011 Merged Topobathy DEM, 2023. 2009–2011 CA Coastal Conservancy Coastal Lidar Project: Hydro-Flattened Bare Earth DEM from 2010 to 06-15 to 2010-08-15. Available online: <https://www.fisheries.noaa.gov/inport/item/55761> (accessed on 22 May 2023).
52. NOAA. 2014 USACE NCMP Topobathy Lidar DEM: California, 2023. Collected by the Joint Airborne Lidar Bathymetry Technical Center of Expertise (JALBTCX), Depicting the Elevations above and below the Immediate Coastal Waters. Available online: <https://www.fisheries.noaa.gov/inport/item/49416> (accessed on 22 May 2023).
53. Martyr-Koller, R.; Kernkamp, H.; van Dam, A.; van der Wegen, M.; Lucas, L.; Knowles, N.; Jaffe, B.; Fregoso, T. Application of an unstructured 3D finite volume numerical model to flows and salinity dynamics in the San Francisco Bay-Delta. *Estuar. Coast. Shelf Sci.* **2017**, *192*, 86–107. [CrossRef]
54. Kumbier, K.; Cabral Carvalho, R.; Vafeidis, A.T.; Woodroffe, C.D. Investigating compound flooding in an estuary using hydrodynamic modelling: A case study from the Shoalhaven River, Australia. *Nat. Hazards Earth Syst. Sci.* **2018**, *18*, 463–477. [CrossRef]
55. Lyddon, C.E.; Brown, J.M.; Leonardi, N.; Plater, A.J. Increased coastal wave hazard generated by differential wind and wave direction in hyper-tidal estuaries. *Estuar. Coast. Shelf Sci.* **2019**, *220*, 131–141. [CrossRef]
56. Lyddon, C.E.; Brown, J.M.; Leonardi, N.; Saulter, A.; Plater, A.J. Quantification of the uncertainty in coastal storm hazard predictions due to wave-current interaction and wind forcing. *Geophys. Res. Lett.* **2019**, *46*, 14576–14585. [CrossRef]
57. Serafin, K.A.; Ruggiero, P.; Parker, K.; Hill, D.F. What's streamflow got to do with it? A probabilistic simulation of the competing oceanographic and fluvial processes driving extreme along-river water levels. *Nat. Hazards Earth Syst. Sci.* **2019**, *19*, 1415–1431. [CrossRef]
58. Kvočka, D.; Falconer, R.A.; Bray, M. Appropriate model use for predicting elevations and inundation extent for extreme flood events. *Nat. Hazards* **2015**, *79*, 1791–1808. [CrossRef]
59. Costabile, P.; Costanzo, C.; De Lorenzo, G.; Macchione, F. Is local flood hazard assessment in urban areas significantly influenced by the physical complexity of the hydrodynamic inundation model? *J. Hydrol.* **2020**, *580*, 124231. [CrossRef]
60. Wang, J.; Gao, W.; Xu, S.; Yu, L. Evaluation of the combined risk of sea level rise, land subsidence, and storm surges on the coastal areas of Shanghai, China. *Clim. Chang.* **2012**, *115*, 537–558. [CrossRef]
61. Uddin, M.; Alam, J.B.; Khan, Z.H.; Hasan, G.J.; Rahman, T. Two dimensional hydrodynamic modelling of Northern Bay of Bengal coastal waters. *Comput. Water Energy Environ. Eng.* **2014**, *2014*, 49792. [CrossRef]
62. Thanh, V.Q.; Reyns, J.; Wackerman, C.; Eidam, E.F.; Roelvink, D. Modelling suspended sediment dynamics on the subaqueous delta of the Mekong River. *Cont. Shelf Res.* **2017**, *147*, 213–230. [CrossRef]
63. Green, R.H.; Lowe, R.J.; Buckley, M.L. Hydrodynamics of a tidally forced coral reef atoll. *J. Geophys. Res. Oceans* **2018**, *123*, 7084–7101. [CrossRef]
64. Symonds, A.M.; Vijverberg, T.; Post, S.; van der Spek, B.J.; Henrotte, J.; Sokolewicz, M. Comparison between mike 21 FM, delft3d and delft3d FM flow models of western port bay, Australia. *Coast. Eng.* **2016**, *2*, 1–12. [CrossRef]
65. Kramer, S.C.; Stelling, G.S. A conservative unstructured scheme for rapidly varied flows. *Int. J. Numer. Methods Fluids* **2008**, *58*, 183–212. [CrossRef]
66. Akoh, R.; Ishikawa, T.; Kojima, T.; Tomaru, M.; Maeno, S. High-resolution modeling of tsunami run-up flooding: A case study of flooding in Kamaishi city, Japan, induced by the 2011 Tohoku tsunami. *Nat. Hazards Earth Syst. Sci.* **2017**, *17*, 1871–1883. [CrossRef]
67. Xie, D.; Zou, Q.P.; Mignone, A.; MacRae, J.D. Coastal flooding from wave overtopping and sea level rise adaptation in the northeastern USA. *Coast. Eng.* **2019**, *150*, 39–58. [CrossRef]
68. Rong, Y.; Zhang, T.; Zheng, Y.; Hu, C.; Peng, L.; Feng, P. Three-dimensional urban flood inundation simulation based on digital aerial photogrammetry. *J. Hydrol.* **2020**, *584*, 124308. [CrossRef]
69. Liu, Q.; Xu, H.; Wang, J. Assessing tropical cyclone compound flood risk using hydrodynamic modelling: A case study in Haikou City, China. *Nat. Hazards Earth Syst. Sci.* **2022**, *22*, 665–675. [CrossRef]
70. Leroy, S.; Pedreros, R.; André, C.; Paris, F.; Lecacheux, S.; Marche, F.; Vinchon, C. Coastal flooding of urban areas by overtopping: Dynamic modelling application to the Johanna storm (2008) in Gâvres (France). *Nat. Hazards Earth Syst. Sci.* **2015**, *15*, 2497–2510. [CrossRef]
71. Kernkamp, H.W.; Van Dam, A.; Stelling, G.S.; de Goede, E.D. Efficient scheme for the shallow water equations on unstructured grids with application to the Continental Shelf. *Ocean Dyn.* **2011**, *61*, 1175–1188. [CrossRef]

72. Gallegos, H.A.; Schubert, J.E.; Sanders, B.F. Two-dimensional, high-resolution modeling of urban dam-break flooding: A case study of Baldwin Hills, California. *Adv. Water Resour.* **2009**, *32*, 1323–1335. [\[CrossRef\]](#)
73. Bricker, J.D.; Gibson, S.; Takagi, H.; Imamura, F. On the need for larger Manning's roughness coefficients in depth-integrated tsunami inundation models. *Coast. Eng. J.* **2015**, *57*, 1550005. [\[CrossRef\]](#)
74. Schubert, J.E.; Sanders, B.F.; Smith, M.J.; Wright, N.G. Unstructured mesh generation and landcover-based resistance for hydrodynamic modeling of urban flooding. *Adv. Water Resour.* **2008**, *31*, 1603–1621. [\[CrossRef\]](#)
75. Brown, J.D.; Spencer, T.; Moeller, I. Modeling storm surge flooding of an urban area with particular reference to modeling uncertainties: A case study of Canvey Island, United Kingdom. *Water Resour. Res.* **2007**, *43*. [\[CrossRef\]](#)
76. Lyddon, C.; Brown, J.M.; Leonardi, N.; Plater, A.J. Flood hazard assessment for a hyper-tidal estuary as a function of tide-surge-morphology interaction. *Estuaries Coasts* **2018**, *41*, 1565–1586. [\[CrossRef\]](#)
77. Lyddon, C.; Brown, J.M.; Leonardi, N.; Plater, A.J. Uncertainty in estuarine extreme water level predictions due to surge-tide interaction. *PLoS ONE* **2018**, *13*, e0206200. [\[CrossRef\]](#)
78. Poulter, B.; Halpin, P.N. Raster modelling of coastal flooding from sea-level rise. *Int. J. Geogr. Inf. Sci.* **2008**, *22*, 167–182. [\[CrossRef\]](#)
79. Reeve, D.; Soliman, A.; Lin, P. Numerical study of combined overflow and wave overtopping over a smooth impermeable seawall. *Coast. Eng.* **2008**, *55*, 155–166. [\[CrossRef\]](#)
80. Anselme, B.; Durand, P.; Thomas, Y.F.; Nicolae-Lerma, A. Storm extreme levels and coastal flood hazards: A parametric approach on the French coast of Languedoc (district of Leucate). *C. R. Geosci.* **2011**, *343*, 677–690. [\[CrossRef\]](#)
81. Lee, S.; Kang, T.; Sun, D.; Park, J.J. Enhancing an analysis method of compound flooding in coastal areas by linking flow simulation models of coasts and watershed. *Sustainability* **2020**, *12*, 6572. [\[CrossRef\]](#)
82. Zheng, Y.; Sun, H. An Integrated Approach for the Simulation Modeling and Risk Assessment of Coastal Flooding. *Water* **2020**, *12*, 2076. [\[CrossRef\]](#)
83. Bilske, M.; Hagen, S. Defining flood zone transitions in low-gradient coastal regions. *Geophys. Res. Lett.* **2018**, *45*, 2761–2770. [\[CrossRef\]](#)
84. Nash, J.E.; Sutcliffe, J.V. River flow forecasting through conceptual models part I—A discussion of principles. *J. Hydrol.* **1970**, *10*, 282–290. [\[CrossRef\]](#)
85. Thompson, C.M.; Frazier, T.G. Deterministic and probabilistic flood modeling for contemporary and future coastal and inland precipitation inundation. *Appl. Geogr.* **2014**, *50*, 1–14. [\[CrossRef\]](#)
86. Lian, J.; Xu, K.; Ma, C. Joint impact of rainfall and tidal level on flood risk in a coastal city with a complex river network: A case study of Fuzhou City, China. *Hydrol. Earth Syst. Sci.* **2013**, *17*, 679–689. [\[CrossRef\]](#)
87. Xu, K.; Ma, C.; Lian, J.; Bin, L. Joint probability analysis of extreme precipitation and storm tide in a coastal city under changing environment. *PLoS ONE* **2014**, *9*, e109341. [\[CrossRef\]](#)
88. Tu, X.; Du, Y.; Singh, V.P.; Chen, X. Joint distribution of design precipitation and tide and impact of sampling in a coastal area. *Int. J. Climatol.* **2018**, *38*, e290–e302. [\[CrossRef\]](#)
89. Lucey, J.T.; Gallien, T.W. Compound coastal flood risk in a semi-arid urbanized region: The implications of copula choice, sampling, and infrastructure. *Nat. Hazards Earth Syst. Sci. Discuss.* **2021**, 1–33. [\[CrossRef\]](#)
90. Schwarz, G. Estimating the dimension of a model. *Ann. Stat.* **1978**, *6*, 461–464.
91. Sadegh, M.; Moftakhari, H.; Gupta, H.V.; Ragno, E.; Mazdiyasni, O.; Sanders, B.; Matthew, R.; AghaKouchak, A. Multihazard scenarios for analysis of compound extreme events. *Geophys. Res. Lett.* **2018**, *45*, 5470–5480. [\[CrossRef\]](#)
92. Haddad, K.; Rahman, A.; Stedinger, J.R. Regional flood frequency analysis using Bayesian generalized least squares: A comparison between quantile and parameter regression techniques. *Hydrol. Process.* **2012**, *26*, 1008–1021. [\[CrossRef\]](#)
93. Chen, X.; Shao, Q.; Xu, C.Y.; Zhang, J.; Zhang, L.; Ye, C. Comparative study on the selection criteria for fitting flood frequency distribution models with emphasis on upper-tail behavior. *Water* **2017**, *9*, 320. [\[CrossRef\]](#)
94. Orange County Environmental Management Agency. *Orange County Hydrology Manual*; Orange County Environmental Management Agency: Santa Ana, CA, USA, 1986; pp. 1–190. Available online: https://ocip.ocpublicworks.com/sites/ocpwocip/files/2020-12/OC_Hydrology_Manual.pdf (accessed on 22 May 2023).
95. Chow, V.T. *Open-Channel Hydraulics*; McGraw-Hill Civil Engineering Series; McGraw-Hill: New York, NY, USA, 1959.
96. Huang, H.; Cui, H.; Ge, Q. Assessment of potential risks induced by increasing extreme precipitation under climate change. *Nat. Hazards* **2021**, *108*, 2059–2079. [\[CrossRef\]](#)

Disclaimer/Publisher's Note: The statements, opinions and data contained in all publications are solely those of the individual author(s) and contributor(s) and not of MDPI and/or the editor(s). MDPI and/or the editor(s) disclaim responsibility for any injury to people or property resulting from any ideas, methods, instructions or products referred to in the content.